

Cove-edged Chiral Graphene Nanoribbons with Chirality-dependent Bandgap and Carrier Mobility

Kun Liu, Wenhao Zheng, Silvio Osella, Zhenlin Qiu, Steffen Böckmann, Wenhui Niu, Laura Meingast, Hartmut Komber, Sebastian Obermann, Roland Gillen, Mischa Bonn, Michael Ryan Hansen, Janina Maultzsch, Hai I. Wang, Ji Ma, Xinliang Feng

Abstract

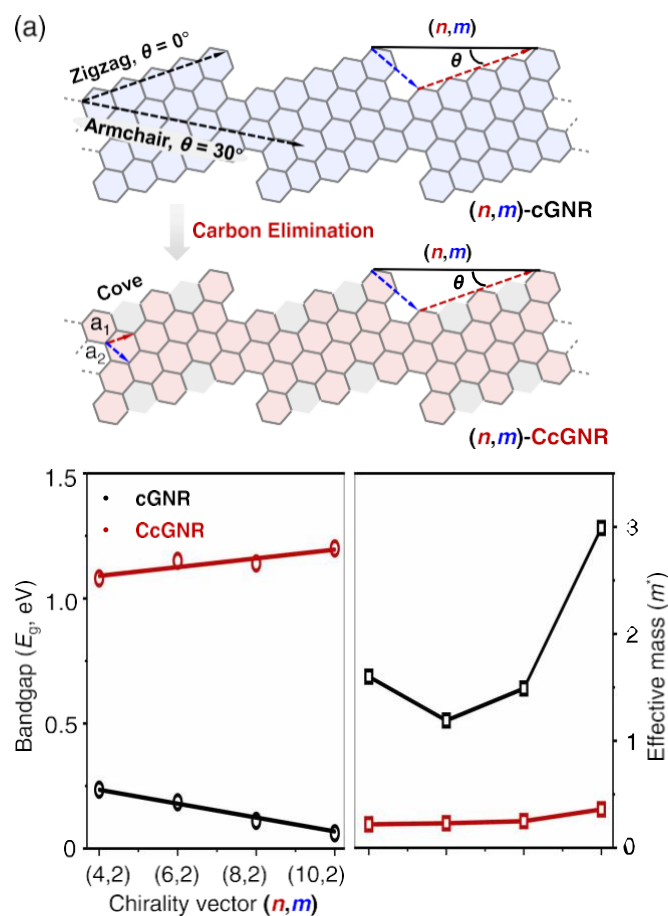
Graphene nanoribbons (GNRs) have garnered significant interest due to their highly customizable physicochemical properties and potential utility in nanoelectronics. Besides controlling widths and edge structures, the inclusion of chirality in GNRs brings another dimension for fine-tuning their optoelectronic properties, but related studies remain elusive owing to the absence of feasible synthetic strategies. Here, we demonstrate a novel class of cove-edged chiral GNRs (CcGNRs) with a tunable chiral vector (n,m) . Notably, the bandgap and effective mass of $(n,2)$ - CcGNR show a distinct positive correlation with the increasing value of n , as indicated by theory. Within this GNR family, two representative members, namely, $(4,2)$ - CcGNR and $(6,2)$ -CcGNR, are successfully synthesized. Both CcGNRs exhibit prominently curved geometries arising from the incorporated [4]helicene motifs along their peripheries, as also evidenced by the single-crystal structures of the two respective model compounds (1 and 2). The chemical identities and optoelectronic properties of

$(4,2)$ - and $(6,2)$ -CcGNRs are comprehensively investigated via a combination of IR, Raman, solid-state NMR, UV-vis, and THz spectroscopies as well as theoretical calculations. In line with theoretical expectation, the obtained $(6,2)$ -CcGNR possesses a low optical bandgap of 1.37 eV along with charge carrier mobility of $\sim 8 \text{ cm}^2 \text{ V}^{-1} \text{ s}^{-1}$, whereas $(4,2)$ -CcGNR exhibits a narrower bandgap of 1.26 eV with increased mobility of $\sim 14 \text{ cm}^2 \text{ V}^{-1} \text{ s}^{-1}$. This work opens up a new avenue to precisely engineer the bandgap and carrier mobility of GNRs by manipulating their chiral vector.

Introduction

Graphene nanoribbons (GNRs) possess enormous potential for next-generation semiconductor materials on account of their tunable bandgaps and attractive electronic properties.¹⁻⁵ In general, the widths and edge topologies of GNRs exert significant influence over their electronic and magnetic properties.^{6,7} Among various methods used to prepare GNRs, bottom-up organic synthesis, utilizing surface-assisted or solution-based chemistry, offers a powerful protocol for fabricating GNRs with structural precision and tailored characteristics.⁸⁻¹² Taking advantage of precision organic synthesis, armchair-edged GNRs (AGNRs) have been widely studied in the past decade, demonstrating a wide range of bandgaps inversely proportional to the ribbon widths. Moreover, zigzag-edged GNRs (ZGNRs) with localized edge states have also been successfully realized via on-surface synthesis under ultrahigh-vacuum conditions.¹³ Besides, chiral GNRs (cGNRs) with combined zigzag and armchair edge orientations represent another important class of GNRs (Figure 1a), which are predicted to possess distinctive properties, such as spin-polarized edge states, chirality-dependent bandgaps, tunable magnetic properties, etc.¹⁴⁻¹⁷ However, experimental access to cGNRs remains relatively rare, and there are only a

few cases prepared using on-surface synthesis,^{18,19} due to the inherent instability associated with the zigzag edges.



(c) This work: synthesis of cove-edged chiral GNRs (CcGNRs)

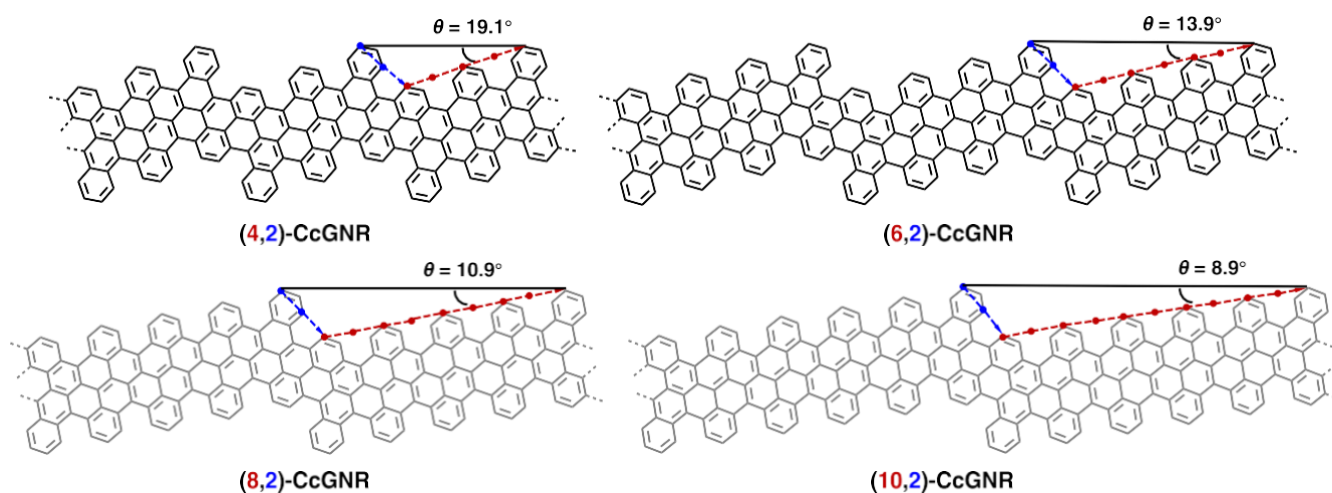


Figure 1. (a) Illustration of pristine (n,m)-cGNRs and the corresponding cove-edged chiral GNRs ((n,m)-CcGNRs) achieved via periodic carbon elimination. The chirality is described either by the translation vector C_h defined as $C_h = na_1 + ma_2$, where n and m are lattice translational indices, a_1 and a_2 are the basis vectors. (b) Comparison of the calculated bandgap and effective mass between (n,m)-CcGNRs and (n,m)-cGNRs (Tables S6 and S7). (c) Chemical structures of four family members in (n,m)-CcGNRs, including the (4,2)-, (6,2)-, (8,2)-, and (10,2)-CcGNR, of which (4,2)- and (6,2)-CcGNR are synthesized in this work. The substituents are omitted for clarity.

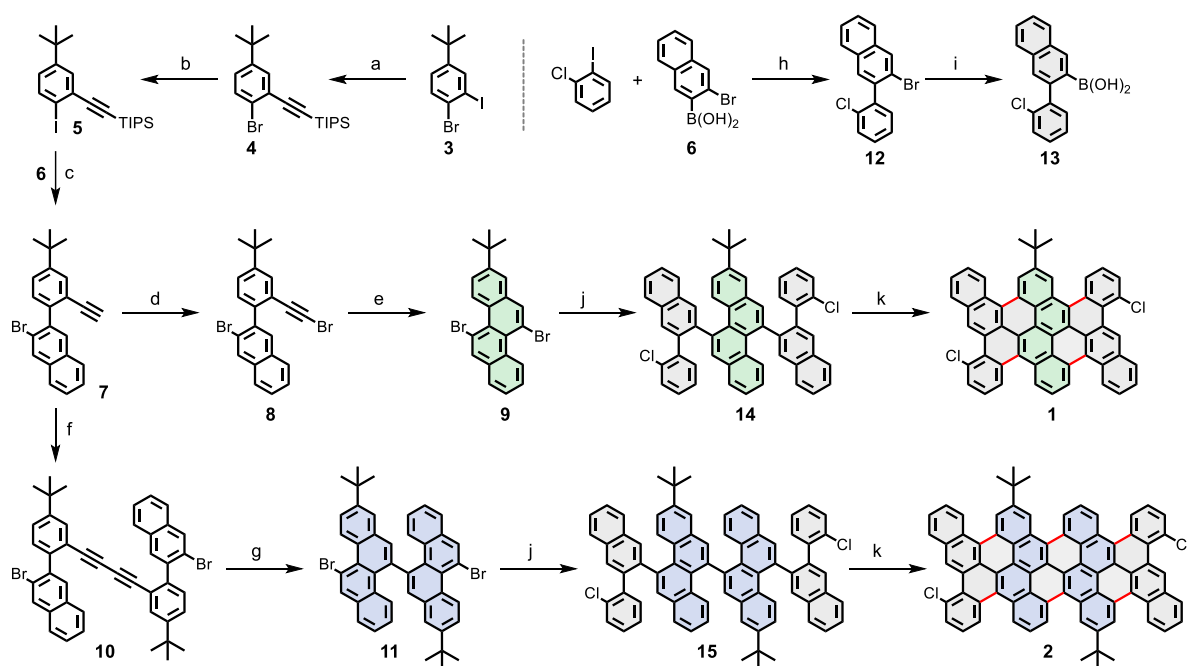
From a structural perspective, by periodically eliminating carbon atoms along the zigzag edges of ZGNR, the [4]helicene subunits (namely, cove edges) are formed on the ZGNR peripheries (Figure 1a), giving rise to a family of cove-edged GNRs (CGNRs) with nonplanar conformation, good liquid-phase processability, and in some cases, low bandgaps and high charge transport properties.^{20–22} Moreover, this “carbon elimination” strategy also has the potential to conquer the stability issue associated with the spin-polarized zigzag edges in GNRs. Inspired by this approach, we envisioned whether it could be applied to the cGNRs with the incorporation of cove edges and subsequently control the stability, geometry, and electronic structures of cGNRs by varying the chiral vector (Figure 1a).^{14,17} To the best of our knowledge, cove-edged chiral GNRs (CcGNRs) have yet to be explored both theoretically and experimentally, representing a novel and untapped area of research. Chirality vector (n,m)

In this work, we report a novel category of chiral GNRs bearing fully cove edges that are realized through the design strategy of “carbon elimination” applied to the backbone of pristine cGNRs by manipulating the chiral vector (n,m) or chiral angle (θ) of cGNRs. Interestingly, theoretical predictions reveal a distinct trend in the bandgap and effective mass of the resulting ($n,2$)-CcGNRs as n evolves, while pristine ($n,2$)-cGNRs display an opposite trend in bandgap evolution and a randomly changing effective mass (Figure 1b). Within this new GNR family, two representative members with the lowest bandgap and effective mass, namely, (4,2)-CcGNR and (6,2)-CcGNR, are successfully synthesized through the Yamamoto polymerization and the subsequent Scholl reaction in solution (Figure 1c). To validate the efficiency of the Scholl reaction, two model compounds 1 and 2 are synthesized as representative fragments of (4,2)-CcGNR and (6,2)-CcGNR, respectively (Scheme 1). Crystallographic analysis of 1 and 2 elucidates their characteristic nonplanar alternative up-down topologies attributed to the steric congestion along the cove peripheries. The successful formation of CcGNRs is confirmed through a combination of infrared (IR), Raman, and solid-state NMR analysis. Increasing the chiral angle θ of ($n,2$)-CcGNRs is theoretically predicted to reduce the bandgap (E_g), which is also validated by experimental comparison of the obtained (4,2)-CcGNR ($\theta = 19.1^\circ$, $E_g = 1.26$ eV) and (6,2)-CcGNR ($\theta = 13.9^\circ$, $E_g = 1.37$ eV) through UV-vis absorption spectroscopy. Furthermore, time-resolved terahertz (THz) spectroscopy unveils a charge carrier mobility of ~ 8.0 cm² V⁻¹ s⁻¹ for (6,2)-CcGNR in dispersion, which notably increased to ~ 14 cm² V⁻¹ s⁻¹ for (4,2)-CcGNR, primarily driven by the enhanced mobility of charge carriers, surpassing that of most solution-synthesized GNRs reported so far.^{23–26} Our study offers new insights into the precise customization of GNR’s bandgap and carrier mobility via tailoring their chirality.

Results and discussion

Design Principle Guided by Theoretical Calculation. As depicted in Figure 1a, the chirality of pristine cGNR is described either by the chiral angle θ or by a chiral vector (n,m), where n and m represent the scalar projections of the vector onto the basis vectors of the graphene lattice. Utilizing the same definition, the corresponding CcGNRs can be derived through periodic carbon elimination along the zigzag edges of cGNRs, where the chiral angle θ gets decreased with increasing n while keeping m unchanged. Following this principle, a family of CcGNRs with same unit width is conceived by varying n and m , in which ($n,2$)-CcGNR is selected as a model to explore the effects of different chirality on their electronic structure. Periodic density

functional theory (DFT) calculations are employed to investigate the evolution of bandgaps and effective masses of $(n,2)$ -CcGNRs by gradually increasing the value of n , in comparison to that of the corresponding $(n,2)$ -cGNRs (Figure 1b). It is found that the value of n significantly modulates the electronic band structure, affecting both the bandgap and band dispersion of $(n,2)$ -CcGNRs (Table S6). All of these CcGNRs exhibited semiconducting behaviour with narrow bandgaps ranging from 1.08 to 1.21 eV when vector n is varied from 4 to 10. The most significant impact is observed in the band dispersion resulting from the alteration in vector n . Notably, the band dispersion near the valence band maximum (VBM) and the conduction band minimum (CBM) exhibits a near-flat profile for $(8,2)$ -CcGNR and $(10,2)$ -CcGNR, while a more pronounced dispersion is observed in $(4,2)$ -CcGNR, which is directly translated into lower values of reduced masses for both hole and electron carriers (m^*_h and m^*_e), thus giving small effective mass (m^*) calculated by $1/m^* = 1/m^*_e + 1/m^*_h$. This characteristic indicates the presence of more extensively delocalized charge carriers in $(4,2)$ -CcGNR. As a result, the bandgap and effective mass values exhibit positive correlations with the increase in n within the $(n,2)$ -CcGNR system (Figure 1b), while that of the pristine cGNRs display the opposite trend with semimetal features (0.06-0.23 eV). Motivated by the aforementioned theoretical findings in this CcGNR family, as well as considering the synthetic feasibility, two representative cases, namely $(4,2)$ -CcGNR and $(6,2)$ -CcGNR, with the narrow bandgaps and low effective masses, were chosen to experimentally investigate the dependency of electronic structures on the GNR chirality (Figure 1c).



Scheme 1. Synthetic Route toward Model Compounds 1 and 2. Regents and conditions: (a) (Triisopropylsilyl)acetylene, CuI, PdCl₂(PPh₃)₂, THF/TEA, r.t., 12 h, 95%; (b) *n*-BuLi, I₂, THF, -78 °C, 16 h, 97%; (c) i. (3-bromonaphthalen-2-yl)boronic acid, Pd(PPh₃)₄, K₂CO₃, THF/EtOH/H₂O, 60 °C, 36 h; ii. TBAF, THF, r.t., 20 min, 79%; (d) NBS, AgNO₃, acetone, r.t., 1 h, 66%; (e) InCl₃, toluene, 95 °C, 24 h, 87%; (f) CuI, piperidine, toluene, Air, r.t., 6 h, 83%; (g) PtCl₂, toluene, 90 °C, 24 h, 93%; (h) 2-chloriodobenzene, Pd(PPh₃)₄, Na₂CO₃, *n*Bu₄NBr, THF/EtOH/H₂O, 60 °C, 10 h, 85%; (i) *n*-BuLi, triisopropyl borate, THF, -78 °C, 16 h, 61%; (j) Pd(PPh₃)₄, K₂CO₃, toluene/EtOH/H₂O, 95 °C, 48 h, 55% for **14** and 60% for **15**; (k) DDQ, TFOH, DCM, 0 °C, 45 min, 62% for **1** and 65% for **2**.

Synthesis and Characterization of Model Compounds. As the defined segments of (4,2)-CcGNR and (6,2)-CcGNR, model compounds **1** and **2** containing chrysene unit were synthesized respectively (Scheme 1). First, ((2-bromo-5-(*tert*-butyl)phenyl)ethynyl)triisopropylsilane (**4**) was prepared in 95% yield by selective Sonogashira coupling of 1-bromo-4-(*tert*-butyl)-2-iodobenzene (**3**) with (triisopropylsilyl)acetylene. Then, compound **4** was transformed into ((5-(*tert*-butyl)-2-iodophenyl)ethynyl)triisopropylsilane (**5**) by treatment with *n*-butyllithium/iodine in 97% yield. Afterward, a Suzuki coupling of **5** with (3-bromonaphthalen-2-yl)boronic acid (**6**) followed by treatment with tetrabutylammonium fluoride (TBAF) provided 2-bromo-3-(4-(*tert*-butyl)-2-ethynylphenyl)naphthalene (**7**) with a yield of 79% over two steps. The bromination of the acetylenic group in **7** afforded 2-bromo-3-(2-(bromoethynyl)-4-(*tert*-butyl)phenyl)naphthalene (**8**) in 66% yield. Subsequently, 5,11-dibromo-2-(*tert*-butyl)chrysene (**9**) was obtained from **8** in 87% yield via InCl_3 -catalyzed alkyne benzannulation. Meanwhile, the Glaser coupling of **7** catalyzed by copper iodine (CuI) under air condition gave 1,4-bis(2-(3-bromonaphthalen-2-yl)-5-(*tert*-butyl)phenyl)buta-1,3-diyne (**10**) in 83% yield and the subsequent platinum chloride (PtCl_2)-catalyzed annulation gave the 11,11'-dibromo-5,5'-bischrysene (**11**) in 93% yield. Furthermore, a Suzuki coupling of the commercially available 2-chloriodobenzene and **6** followed by lithiation/borylation gave (3-(2-chlorophenyl)naphthalen-2-yl)boronic acid (**13**) in 52% yield over two steps. After that, the chrysene-based oligomer precursor **14** and the extended precursor **15** were synthesized via twofold Suzuki coupling in 55% and 60% yield, respectively. Finally, the Scholl reaction of **14** was carried out by using 2,3-dichloro-5,6-dicyano-1,4-benzoquinone (DDQ)/trifluoromethanesulfonic acid ($\text{CF}_3\text{SO}_3\text{H}$), affording the desired model compounds **1** with a yield of 65%. Following the similar synthetic strategy, model compound **2** was also obtained with a yield of 62% from the precursor **15** via the same Scholl reaction condition.

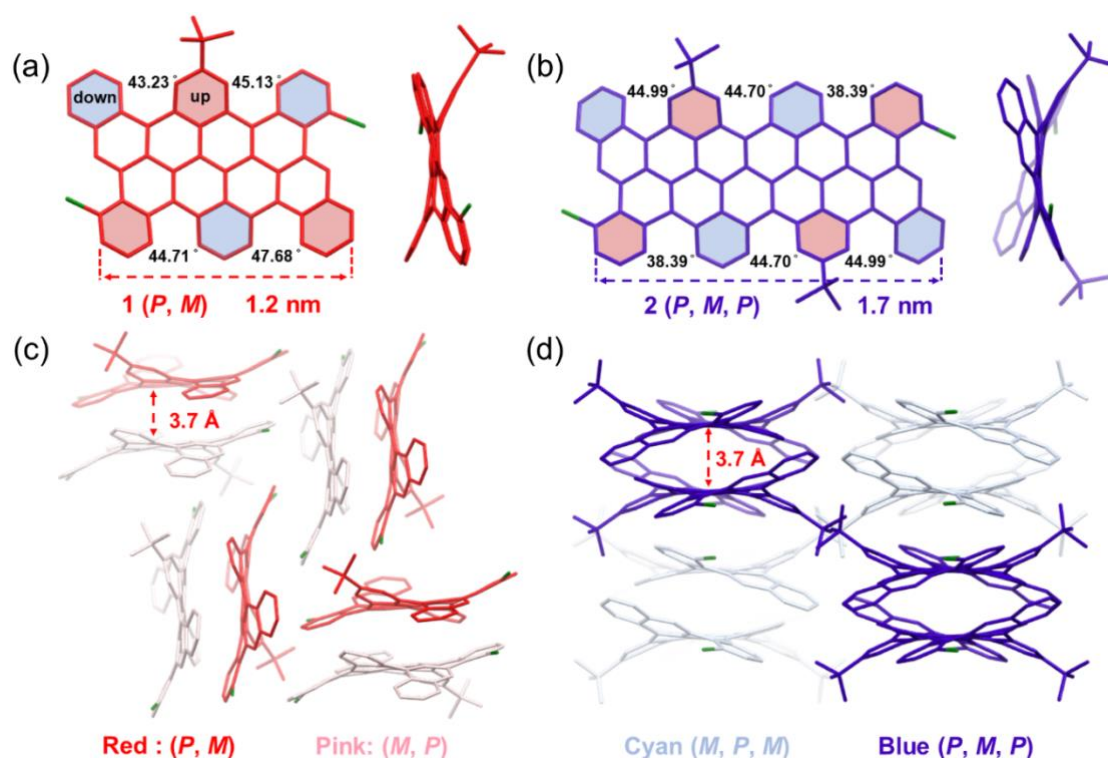
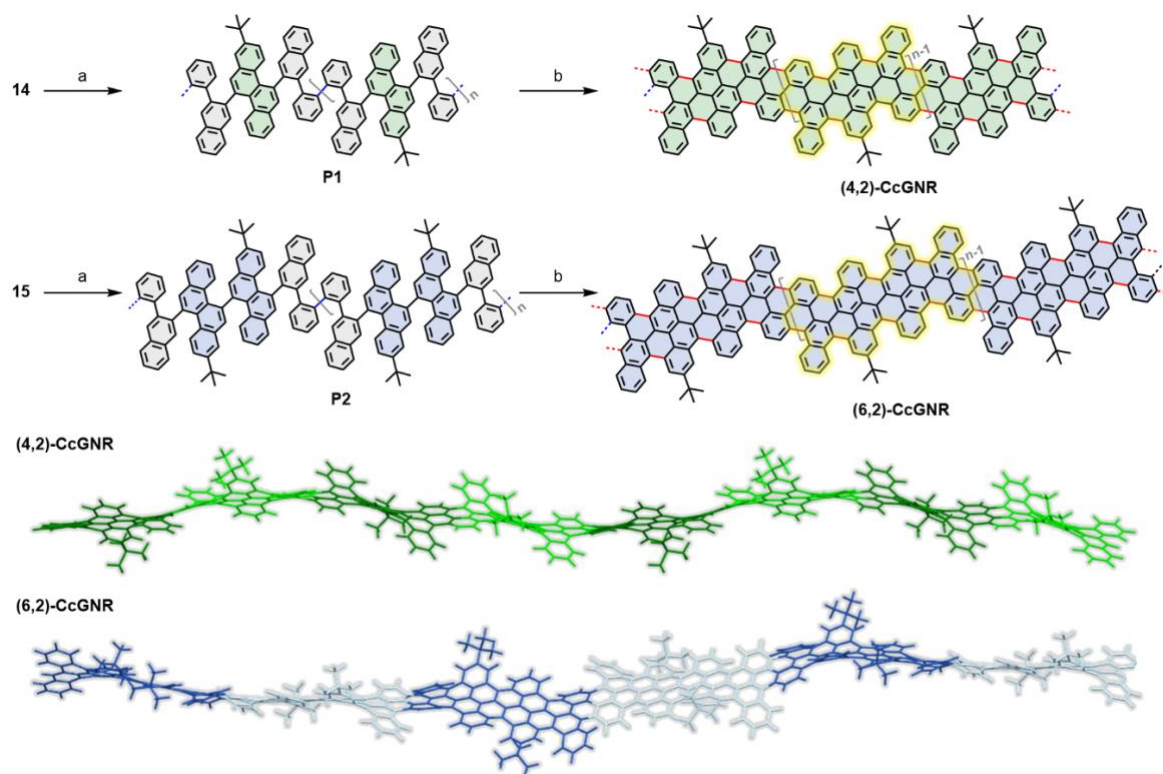


Figure 2. Crystal structures of **1** and **2**. (a, b) Top and side views of **1** (*P, M*) and **2** (*P, M, P*). (c, d) Side view of the crystal packing of **1** and **2**. Hydrogen atoms and solvent molecules are omitted for clarity.

The chemical identities of **1** and **2** were first validated by MALDI-TOF MS analysis, in which the observed spectra were in good agreement with the simulated isotopic distribution patterns (Figure S2). The chemical structure of **1** was further demonstrated by ^1H NMR spectroscopy with the help of 2D NMR measurements (Figures S45-S48). In contrast, compound **2** exhibited poor solubility and a strong tendency for aggregation in the common organic solvent, resulting in a faint and broad ^1H NMR signal. To our delight, a measurement conducted at 90°C in the aromatic solvent toluene- d_8 gave an evaluable ^1H NMR spectrum (Figures S49-S51). Single crystals of **1** and **2** were obtained, respectively, by slow vapor diffusion of methanol into a solution of compound **1** in dichloroethane and a solution of compound **2** in chlorobenzene, which are suitable for single-crystal X-ray diffraction measurements (Figure 2). Compound **1** crystallized in the orthorhombic space group $Pna2_1$, while **2** crystallized in the monoclinic space group $C2/c$ (Table S1). As shown in Figure 2a,b, both **1** and **2** possess alternating “up-down” geometries with the large torsion angles within the cove regions ($43.23\text{--}47.68^\circ$ for **1** and $38.39\text{--}44.99^\circ$ for **2**) owing to the steric repulsion resulting from the [4]helicene segments at the peripheries. Consequently, elongated C–C bonds ($1.42\text{--}1.48\text{ \AA}$ for **1** and $1.40\text{--}1.51\text{ \AA}$ for **2**) at the cove edges are afforded, which are comparable with those of the reported cove-edged nanographenes.^{27,28} In the solid packing, two enantiomers (*(P, M, P, M)* and *(M, P, M, P)* for **1** and *(P, M, P, P, M, P)* and *(M, P, M, M, P, M)* for **2**) are present in a ratio of 1:1 in the unit cell (Figure 2c,d). Notably, the unsymmetrically substituted **1** form racemic dimers by face-to-face $\pi\text{--}\pi$ interactions with an interlayer distance of 3.7 \AA , whereas such dimers further self-assemble by face-to-edge $[\text{C--H}\cdots\pi]$ interactions.²⁹ In contrast, each enantiomer of **2** forms dimers by intermolecular $\pi\text{--}\pi$ interactions with a similar distance of 3.7 \AA , which undergo brick layer stacking along the *b*-axis by aligning with another pair of enantiomeric isomers via $\pi\text{--}\pi$ interactions.



Scheme 2. Synthesis of (4,2)-CcGNR and (6,2)-CcGNR as well as their DFT optimized geometries. Regents and conditions: (a) Ni(COD)₂, COD, 2,2'-bipyridine, toluene/DMF, 80 °C, 3 days, 85% for **P1** and 89% for **P2**; (b) DDQ, TfOH, DCM, 0 °C to r.t., 2 days, 86% for (4,2)-CcGNR and 89% for (6,2)-CcGNR. The repeating unit is highlighted in yellow color.

Synthesis and Characterization of (4,2)-CcGNR and (6,2)-CcGNR. After the efficient synthesis of model compounds was confirmed, the syntheses of (4,2)-CcGNR and (6,2)-CcGNR are further investigated. With the building blocks 14 and 15 in hand, nickel-mediated Yamamoto polymerization provided the desired polyphenylene precursors **P1** and **P2** in 85 and 89% yields, respectively (Scheme 2). Linear mode MALDI-TOF MS analysis of the crude polymers **P1** and **P2** reveals a family of signals up to $m/z \sim 9.600$ and 10.700 , spaced by the repetition unit of 686 and 968 g mol^{-1} , respectively (Figure 3a). The obtained crude polymers were then fractionated into three fractions by recycling gel permeation chromatography (GPC), followed by the analysis of analytical size exclusion chromatography (SEC) calibrated by polystyrene (PS) standards. The analysis revealed a close number-average molar mass of $M_n \sim 10.200 \text{ Da}$ with a low polydispersity index (D) for the first fraction of both polymers with the highest molecular weight ($D = 1.06$ for **P1**, $D = 1.05$ for **P2**) (Figures S3 and S4). Finally, oxidative cyclodehydrogenation of the obtained fractions of **P1** and **P2** through the Scholl reaction in DCM with DDQ/TfOH at 0 °C for 2 days yield the targeted (4,2)-CcGNR and (6,2)-CcGNR with yields of 86 and 89%, respectively. The average length of the high-molecular-weight fraction of the resulting (4,2)- and (6,2)-CcGNR is estimated to be 21 nm, based on the M_n of the corresponding **P1** and **P2** precursors and on the length of the repeat unit estimated from the crystal structures of 1 and 2 (Figure 2a,b). Thanks to their curved geometries and the *tert*-butyl substituents installed on the ribbon edges, both GNRs exhibited good dispersibility in common organic solvents, such as *N*-methyl-2-pyrrolidone (NMP), tetrahydrofuran, and 1,2,4-trichlorobenzene.

The successful conversion of polymer precursors P1 and P2 into (4,2)-CcGNR and (6,2)-CcGNR was verified through a comprehensive analysis involving IR, Raman, and solid-state NMR spectroscopies. A comparison of the IR spectra of P1 and (4,2)-CcGNR revealed that the C–H stretching vibrations at 3025 and 3053 cm^{-1} in P1 were diminished after cyclodehydrogenation, whereas a very broad maximum was present close to 3024 cm^{-1} (Figure 3b).^{2,30,31} Furthermore, the out-of-plane (*opla*) C–H deformation bands triad at 698 and 744 cm^{-1} (pink and green) originating from disubstituted aromatic rings was attenuated after graphitization, while a strong band associated with TRIO and QUATRO modes (wagging of triply or quadruply adjacent C–H groups, identified by comparison to the HSEH1PBE/6-31G(d) prediction (Tables S2–S4)) can be found at 755 cm^{-1} (blue) in (4,2)-CcGNR.^{31,32} These observations were in line with the variation in the IR spectra of polymers P2 and (6,2)-CcGNR as well, where the C–H stretching region at 3052 cm^{-1} and the fingerprint bands at 697 and 744 cm^{-1} were diminished instead of the presence of a joint TRIO and QUATRO mode at 759 cm^{-1} . Moreover, Raman spectra of (4,2)-CcGNR and (6,2)-CcGNR show vibrational modes in the ranges of 150–500 cm^{-1} (inset in Figure 3c), 1000–2000, and 2250–3500 cm^{-1} (Figure 3c), which are confirmed by DFT calculations of the vibrational modes. As the symmetry of the GNR structure is broken by the staircase formation along the nanoribbon axis, there is no symmetry-defined direction of motion of the atoms. Indeed, the calculated vibrations are mixed displacements of different parts of the nanoribbon. In agreement with our experimental results, a characteristic vibrational mode that distinguishes the two nanoribbon structures is not observed in the calculated response. This is probably due to the similarity in the atomic structures of (4,2)-CcGNR and (6,2)-CcGNR. The DFT simulations revealed that the typical vibrational patterns around 1600 cm^{-1} resemble that of the G mode in graphene/graphite^{33,34} (Figure S13a). The lattice vibrations around 1350 cm^{-1} are similar to the vibration leading to the D mode in graphene/graphite^{33,34} but include also vibrational contributions of the CH₃ groups at the edges (Figures S13b,c). Moreover, the solid-state magic-angle spinning (MAS) NMR measurements (Figures S14–S16) confirm the successful graphitization of both polymer P1 and P2 toward corresponding (4,2)-CcGNR and (6,2)-CcGNR, in which ¹H and ¹³C{¹H} MAS NMR display the broadened signals as a consequence of higher dipolar couplings due to the reduced mobility as well as a broader distribution of isotropic chemical shifts as shown by 2D correlation spectroscopy (Figure S16).

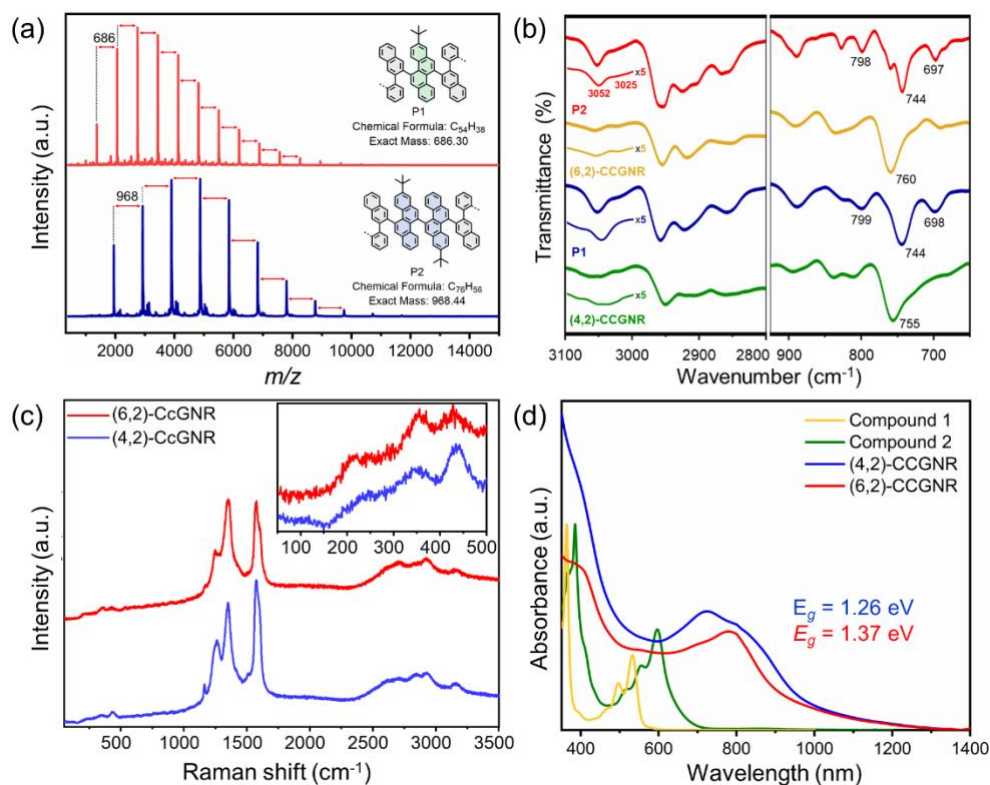


Figure 3. Spectroscopic characterizations of (4,2)-CcGNR and (6,2)-CcGNR. (a) MALDI-TOF MS analysis of polymer **P1** and **P2** (matrix: DCTB, linear mode). (b) FTIR spectra of **P1**, **P2**, (4,2)-CcGNR and (6,2)-CcGNR. (c) Raman spectra of (4,2)-CcGNR and (6,2)-CcGNR measured at 532 nm excitation wavelength. (d) UV-vis absorption spectra of model compounds **1** and **2** in CH_2Cl_2 (10^{-5} M), (4,2)-CcGNR and (6,2)-CcGNR in NMP.

Optical Properties of 1, 2, (4,2)-CcGNR, and (6,2)-CcGNR. Furthermore, the UV-vis absorption spectra of model compounds **1** and **2** in DCM, as well as the (4,2)-CcGNR and (6,2)-CcGNR dispersed in NMP, are recorded in [Figure 3d](#). For compound **1**, a distinct absorption peak with the longest wavelength was observed at 533 nm, corresponding to an optical bandgap of 2.25 eV. Compared to that of **1**, compound **2** exhibited an obvious red-shifted absorption peak at 597 nm with an optical gap of 1.98 eV due to its extended π -conjugation. In stark contrast, (4,2)-CcGNR displayed considerable bathochromic shift in the absorption toward the NIR region with an absorption maximum at 725 nm and a shoulder peak at 802 nm, while extended (6,2)-CcGNR exhibited an absorption maximum at 781 nm. Based on the Tauc plot method for a direct transition (inset in [Figure 3d](#)), the optical bandgap of (4,2)-CcGNR was determined to be 1.26 eV, which is approximately 0.11 eV smaller than the optical bandgap (1.37 eV) of (6,2)-CcGNR. This result aligns with the trend observed in the DFT-calculated bandgaps ([Figure 1b](#)), which also showed a difference of 0.07 eV between (4,2)-CcGNR (1.08 eV) and (6,2)-CcGNR (1.15 eV) ([Table S6](#)).

Charge Carrier Transport Properties of (4,2)-CcGNR and (6,2)-CcGNR. We then examined the charge carrier transport characteristics of the obtained GNRs employing ultrafast optical pump-terahertz probe (OPTP) spectroscopy.³⁵⁻³⁸ In [Figure 4a](#), we present the time-

resolved complex (0.22 m_0 and 0.23 m_0 for (4,2)-CcGNR and (6,2)-CcGNR by taking contributions from both electrons and holes (Figure 1b)), we estimate the charge mobility in the dc limit $\mu_{dc} (= \frac{e\tau}{m^*} (1 + c))$ of 14.3 ± 0.7 and $8.3 \pm 0.5 \text{ cm}^2 \text{ V}^{-1} \text{ S}^{-1}$ for (4,2)-CcGNR and (6,2)-CcGNR, respectively. The relatively high inferred charge carrier mobility in (4,2)-CcGNR, compared with that in (6,2)-CcGNR, indicates the substantial influence of chirality in dictating the charge carrier transport within GNRs.

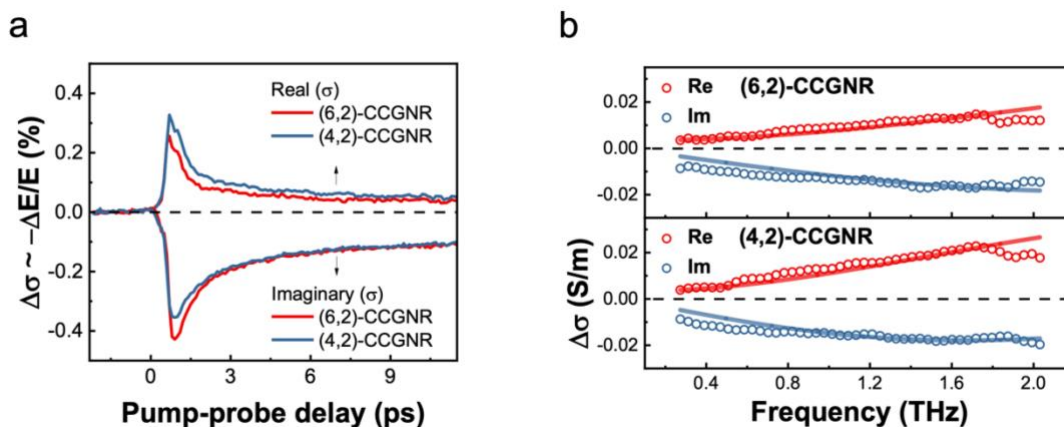


Figure 4. (a) Time-resolved complex terahertz photoconductivity of both (4,2)-CcGNR and (6,2)-CcGNR. (b) Frequency-resolved terahertz conductivity measured at ~ 1.5 ps after photoexcitation. The solid lines are fits to the Drude–Smith model.

Conclusion

In summary, we have introduced a novel family of chiral GNRs featured by the cove edge structures, wherein their bandgap and effective mass exhibit chirality-dependent behavior. Within this family, the successful synthesis of two key members, namely, (4,2)-CcGNR and (6,2)-CcGNR was achieved in solution. Two model compounds 1 and 2 were also synthesized to elucidate the structural features of the corresponding CcGNRs, revealing distinct curved geometries resulting from embedded [4]helicene motifs along the edges. The obtained CcGNRs were comprehensively characterized by IR, Raman, and solid-state NMR techniques. According to DFT calculations, in contrast to pristine cGNRs that have semimetallic characteristics and large effective masses, CcGNRs possess narrow bandgaps and relatively small effective masses that are positively correlated with increasing values of n . Experimentally, both resulting (4,2)-CcGNR and (6,2)-CcGNR exhibited narrow optical bandgaps of 1.26 and 1.37 eV, contingent upon the chiral vector (n,m) , in alignment with theoretical predictions. Moreover, the charge carrier mobility underwent substantial enhancement, increasing from $\sim 8 \text{ cm}^2 \text{ V}^{-1} \text{ s}^{-1}$ for (6,2)-CcGNR to $\sim 14 \text{ cm}^2 \text{ V}^{-1} \text{ s}^{-1}$ for (4,2)-CcGNR. This study presents a promising avenue for manipulating GNR bandgaps and carrier mobility through chirality modification, thereby greatly expanding the range of potential candidates within the GNR family for integration into nanoelectronics.

Supporting Information

The Supporting Information is available free of charge at <https://pubs.acs.org/doi/10.1021/jacs.3c11975>.

Synthetic procedures and characterization data, additional optical spectra of model compounds and polymer precursors, solid-state NMR analysis, DFT calculation details, and NMR spectra of new compounds.

Author Contributions

The manuscript was written through contributions of all authors. All authors have given approval to the final version of the manuscript

Acknowledgements

This research was financially supported by the EU Graphene Flagship (Graphene Core 3, 881603), ERC Consolidator Grant (T2DCP, 819698), H2020-MSCA-ITN (ULTIMATE, No. 813036), the Center for Advancing Electronics Dresden (cfaed), and H2020-EU.1.2.2.-FET Proactive Grant (LIGHT-CAP, 101017821). The authors gratefully acknowledge the GWK support for funding this project by providing computing time through the Center for Information Services and HPC (ZIH) at TU Dresden. S.O. thanks the National Science Centre, Poland (grant no. UMO/2020/39/I/ST4/01446). The computation was carried out with the support of the Interdisciplinary Center for Mathematical and Computational Modeling at the University of Warsaw (ICM UW) under grant nos. G83-28 and GB80-24. L.M., R.G., and J. Maultzsch acknowledge support by the Deutsche Forschungsgemeinschaft (DFG, German Research Foundation)—project numbers 447264071 (INST 90/1183-1 FUGG), 182849149 (SFB 953, B13), and 491865171 (GRK 2861). R.G., L.M., and J. Maultzsch also acknowledge the scientific support and HPC resources provided by the Erlangen National High Performance Computing Center (NHR@FAU) of the FAU under the NHR project b181dc. NHR funding is provided by federal and Bavarian state authorities. NHR@FAU hardware is partially funded by the German Research Foundation (DFG)—440719683.

References

- (1) Li, X.; Wang, X.; Zhang, L.; Lee, S.; Dai, H. Chemically Derived, Ultrasoft Graphene Nanoribbon Semiconductors. *Science* **2008**, *319*, 1229–1232.
- (2) Jiao, L.; Zhang, L.; Wang, X.; Diankov, G.; Dai, H. Narrow Graphene Nanoribbons from Carbon Nanotubes. *Nature* **2009**, *458*, 877–880.
- (3) Nakada, K.; Fujita, M.; Dresselhaus, G.; Dresselhaus, M. S. Edge State in Graphene Ribbons: Nanometer Size Effect and Edge Shape Dependence. *Phys. Rev. B* **1996**, *54*, 17954–17961.
- (4) Cai, J.; Ruffieux, P.; Jaafar, R.; Bieri, M.; Braun, T.; Blankenburg, S.; Muoth, M.; Seitsonen, A. P.; Saleh, M.; Feng, X.; Müllen, K.; Fasel, R. Atomically Precise Bottom-up Fabrication of Graphene Nanoribbons. *Nature* **2010**, *466*, 470–473.
- (5) Narita, A.; Wang, X.-Y.; Feng, X.; Müllen, K. New Advances in Nanographene Chemistry. *Chem. Soc. Rev.* **2015**, *44*, 6616–6643.
- (6) Magda, G. Z.; Jin, X.; Hagymási, I.; Vancsó, P.; Osváth, Z.; Nemes-Incze, P.; Hwang, C.; Biró, L. P.; Tapasztó, L. Room-Temperature Magnetic Order on Zigzag Edges of Narrow Graphene Nanoribbons. *Nature* **2014**, *514*, 608–611.

- (7) Houtsma, R. S. K.; de la Rie, J.; Stöhr, M. Atomically Precise Graphene Nanoribbons: Interplay of Structural and Electronic Properties. *Chem. Soc. Rev.* **2021**, *50*, 6541–6568.
- (8) Yang, X.; Dou, X.; Rouhanipour, A.; Zhi, L.; Räder, H. J.; Müllen, K. Two-Dimensional Graphene Nanoribbons. *J. Am. Chem. Soc.* **2008**, *130*, 4216–4217.
- (9) Narita, A.; Feng, X.; Hernandez, Y.; Jensen, S. A.; Bonn, M.; Yang, H.; Verzhbitskiy, I. A.; Casiraghi, C.; Hansen, M. R.; Koch, A. H. R.; Fytas, G.; Ivasenko, O.; Li, B.; Mali, K. S.; Balandina, T.; Mahesh, S.; De Feyter, S.; Müllen, K. Synthesis of Structurally Well-Defined and Liquid-Phase-Processable Graphene Nanoribbons. *Nat. Chem.* **2014**, *6*, 126–132.
- (10) von Kugelgen, S.; Piskun, I.; Griffin, J. H.; Eckdahl, C. T.; Jarenwattananon, N. N.; Fischer, F. R. Templated Synthesis of End-Functionalized Graphene Nanoribbons through Living Ring-Opening Alkyne Metathesis Polymerization. *J. Am. Chem. Soc.* **2019**, *141*, 11050–11058.
- (11) Niu, W.; Ma, J.; Soltani, P.; Zheng, W.; Liu, F.; Popov, A. A.; Weigand, J. J.; Komber, H.; Poliani, E.; Casiraghi, C.; Droste, J.; Hansen, M. R.; Osella, S.; Beljonne, D.; Bonn, M.; Wang, H. I.; Feng, X.; Liu, J.; Mai, Y. A Curved Graphene Nanoribbon with Multi-Edge Structure and High Intrinsic Charge Carrier Mobility. *J. Am. Chem. Soc.* **2020**, *142*, 18293–18298.
- (12) Yao, X.; Zheng, W.; Osella, S.; Qiu, Z.; Fu, S.; Schollmeyer, D.; Müller, B.; Beljonne, D.; Bonn, M.; Wang, H. I.; Müllen, K.; Narita, A. Synthesis of Nonplanar Graphene Nanoribbon with Fjord Edges. *J. Am. Chem. Soc.* **2021**, *143*, 5654–5658.
- (13) Wang, X.; Ma, J.; Zheng, W.; Osella, S.; Arisnabarreta, N.; Droste, J.; Serra, G.; Ivasenko, O.; Lucotti, A.; Beljonne, D.; Bonn, M.; Liu, X.; Hansen, M. R.; Tommasini, M.; De Feyter, S.; Liu, J.; Wang, H. I.; Feng, X. Cove-Edged Graphene Nanoribbons with Incorporation of Periodic Zigzag-Edge Segments. *J. Am. Chem. Soc.* **2022**, *144*, 228–235.
- (14) Tao, C.; Jiao, L.; Yazyev, O. V.; Chen, Y.-C.; Feng, J.; Zhang, X.; Capaz, R. B.; Tour, J. M.; Zettl, A.; Louie, S. G.; Dai, H.; Crommie, M. F. Spatially Resolving Edge States of Chiral Graphene Nanoribbons. *Nat. Phys.* **2011**, *7*, 616–620.
- (15) Golor, M.; Lang, T. C.; Wessel, S. Quantum Monte Carlo Studies of Edge Magnetism in Chiral Graphene Nanoribbons. *Phys. Rev. B* **2013**, *87*, 155441.
- (16) Sánchez-Sánchez, C.; Dienel, T.; Deniz, O.; Ruffieux, P.; Berger, R.; Feng, X.; Müllen, K.; Fasel, R. Purely Armchair or Partially Chiral: Noncontact Atomic Force Microscopy Characterization of Dibromo-Bianthryl-Based Graphene Nanoribbons Grown on Cu(111). *ACS Nano* **2016**, *10*, 8006–8011.
- (17) Wang, X.-Y.; Urgel, J. I.; Barin, G. B.; Eimre, K.; Di Giovannantonio, M.; Milani, A.; Tommasini, M.; Pignedoli, C. A.; Ruffieux, P.; Feng, X.; Fasel, R.; Müllen, K.; Narita, A. Bottom-Up Synthesis of Heteroatom-Doped Chiral Graphene Nanoribbons. *J. Am. Chem. Soc.* **2018**, *140*, 9104–9107.
- (18) Lawrence, J.; Berdonces-Layunta, A.; Edalatmanesh, S.; Castro-Esteban, J.; Wang, T.; Jimenez-Martin, A.; de la Torre, B.; Castrillo-Bodero, R.; Angulo-Portugal, P.; Mohammed, M. S. G.; Matěj, A.; Vilas-Varela, M.; Schiller, F.; Corso, M.; Jelinek, P.; Peña, D.; de Oteyza, D. G. Circumventing the Stability Problems of Graphene Nanoribbon Zigzag Edges. *Nat. Chem.* **2022**, *14*, 1451–1458.
- (19) Cruz, C. M.; Márquez, I. R.; Mariz, I. F. A.; Blanco, V.; Sánchez-Sánchez, C.; Sobrado, J. M.; Martín-Gago, J. A.; Cuerva, J. M.; Maçôas, E.; Campaña, A. G. Enantiopure Distorted Ribbon-Shaped Nanographene Combining Two-Photon Absorption-Based Upconversion and Circularly Polarized Luminescence. *Chem. Sci.* **2018**, *9*, 3917–3924.
- (20) Verbiest, T.; Elshocht, S. V.; Kauranen, M.; Hellemans, L.; Snauwaert, J.; Nuckolls, C.; Katz, T. J.; Persoons, A. Strong Enhancement of Nonlinear Optical Properties Through Supramolecular Chirality. *Science* **1998**, *282*, 913–915.
- (21) Schuster, N. J.; Joyce, L. A.; Paley, D. W.; Ng, F.; Steigerwald, M. L.; Nuckolls, C. The Structural Origins of Intense Circular Dichroism in a Wagging Helicene Nanoribbon. *J. Am. Chem. Soc.* **2020**, *142*, 7066–7074.

- (22) Dubey, R. K.; Melle-Franco, M.; Mateo-Alonso, A. Twisted Molecular Nanoribbons with up to 53 Linearly-Fused Rings. *J. Am. Chem. Soc.* **2021**, *143*, 6593–6600.
- (23) Miao, D.; Daigle, M.; Lucotti, A.; Boismenu-Lavoie, J.; Tommasini, M.; Morin, J.-F. Toward Thiophene-Annulated Graphene Nanoribbons. *Angew. Chem. Int. Ed.* **2018**, *57*, 3588–3592.
- (24) Xiao, X.; Cheng, Q.; Bao, S. T.; Jin, Z.; Sun, S.; Jiang, H.; Steigerwald, M. L.; Nuckolls, C. Single-Handed Helicene Nanoribbons via Transfer of Chiral Information. *J. Am. Chem. Soc.* **2022**, *144*, 20214–20220.
- (25) Ahmadi, M. T.; Ahmadi, R.; Nguyen, T. K. Graphene Nanoscroll Geometry Effect on Transistor Performance. *J. Electron. Mater.* **2020**, *49*, 544–550.
- (26) Merino-Díez, N.; Li, J.; Garcia-Lekue, A.; Vasseur, G.; Vilas-Varela, M.; Carbonell-Sanromà, E.; Corso, M.; Ortega, J. E.; Peña, D.; Pascual, J. I.; de Oteyza, D. G. Unraveling the Electronic Structure of Narrow Atomically Precise Chiral Graphene Nanoribbons. *J. Phys. Chem. Lett.* **2018**, *9*, 25–30.
- (27) Jiang, Z.; Song, Y. Band Gap Oscillation and Novel Transport Property in Ultrathin Chiral Graphene Nanoribbons. *Phys. B Condens. Matter* **2015**, *464*, 61–67.
- (28) Gu, Y.; Muñoz-Mármol, R.; Wu, S.; Han, Y.; Ni, Y.; Díaz-García, M. A.; Casado, J.; Wu, J. Cove-Edged Nanographenes with Localized Double Bonds. *Angew. Chem.* **2020**, *132*, 8190–8194.
- (29) Gu, Y.; Vega-Mayoral, V.; Garcia-Orrit, S.; Schollmeyer, D.; Narita, A.; Cabanillas-González, J.; Qiu, Z.; Müllen, K. Cove-Edged Hexa-Peri-Hexabenzobis-Peri-Octacene: Molecular Conformations and Amplified Spontaneous Emission. *Angew. Chem. Int. Ed.* **2022**, *61*.
- (30) Centrone, A.; Brambilla, L.; Renouard, T.; Gherghel, L.; Mathis, C.; Müllen, K.; Zerbi, G. Structure of New Carbonaceous Materials: The Role of Vibrational Spectroscopy. *Carbon* **2005**, *43*, 1593–1609.
- (31) Hu, Y.; Xie, P.; De Corato, M.; Ruini, A.; Zhao, S.; Meggendorfer, F.; Straasø, L. A.; Rondin, L.; Simon, P.; Li, J.; Finley, J. J.; Hansen, M. R.; Lauret, J.-S.; Molinari, E.; Feng, X.; Barth, J. V.; Palma, C.-A.; Prezzi, D.; Müllen, K.; Narita, A. Bandgap Engineering of Graphene Nanoribbons by Control over Structural Distortion. *J. Am. Chem. Soc.* **2018**, *140*, 7803–7809.
- (32) Schwab, M. G.; Narita, A.; Hernandez, Y.; Balandina, T.; Mali, K. S.; De Feyter, S.; Feng, X.; Müllen, K. Structurally Defined Graphene Nanoribbons with High Lateral Extension. *J. Am. Chem. Soc.* **2012**, *134*, 18169–18172.
- (33) Zheng, W.; Zorn, N. F.; Bonn, M.; Zaumseil, J.; Wang, H. I. Probing Carrier Dynamics in Sp³-Functionalized Single-Walled Carbon Nanotubes with Time-Resolved Terahertz Spectroscopy. *ACS Nano* **2022**, *16*, 9401–9409.
- (34) Ulbricht, R.; Hendry, E.; Shan, J.; Heinz, T. F.; Bonn, M. Carrier Dynamics in Semiconductors Studied with Time-Resolved Terahertz Spectroscopy. *Rev. Mod. Phys.* **2011**, *83*, 543–586.
- (35) Zheng, W.; Sun, B.; Li, D.; Gali, S. M.; Zhang, H.; Fu, S.; Di Virgilio, L.; Li, Z.; Yang, S.; Zhou, S.; Beljonne, D.; Yu, M.; Feng, X.; Wang, H. I.; Bonn, M. Band Transport by Large Fröhlich Polarons in MXenes. *Nat. Phys.* **2022**, *18*, 544–550.
- (36) Jensen, S. A.; Ulbricht, R.; Narita, A.; Feng, X.; Müllen, K.; Hertel, T.; Turchinovich, D.; Bonn, M. Ultrafast Photoconductivity of Graphene Nanoribbons and Carbon Nanotubes. *Nano Lett.* **2013**, *13*, 5925–5930.
- (37) Tries, A.; Osella, S.; Zhang, P.; Xu, F.; Ramanan, C.; Kläui, M.; Mai, Y.; Beljonne, D.; Wang, H. I. Experimental Observation of Strong Exciton Effects in Graphene Nanoribbons. *Nano Lett.* **2020**, *20*, 2993–3002.
- (38) Cocker, T. L.; Baillie, D.; Buruma, M.; Titova, L. V.; Sydora, R. D.; Marsiglio, F.; Hegmann, F. A. Microscopic Origin of the Drude-Smith Model. *Phys. Rev. B* **2017**, *96*, 205439.